AGU PUBLICATIONS

Journal of Advances in Modeling Earth Systems

RESEARCH ARTICLE
10.1002/2017MS001167

Key Points:
- Monte-Carlo model of the growth of ice particles due to depositional growth, aggregation, and riming
- Large uncertainty of the riming process emphasizes the need for laboratory and field measurements

Correspondence to:
S. Brdar,
s.brdar@fz-juelich.de

Citation:
Brdar, S., & Seifert, A. (2018). McSnow: A Monte-Carlo particle model for riming and aggregation of ice particles in a multidimensional microphysical phase space. *Journal of Advances in Modeling Earth Systems*, *10*, 187–206. https://doi.org/10.1002/2017MS001167

Received 8 SEP 2017
Accepted 14 DEC 2017
Accepted article online 18 DEC 2017
Published online 18 JAN 2018

McSnow: A Monte-Carlo Particle Model for Riming and Aggregation of Ice Particles in a Multidimensional Microphysical Phase Space

S. Brdar[1,2] and A. Seifert[1]

[1]Deutscher Wetterdienst, Offenbach, Germany, [2]Now at Jülich Supercomputing Centre, Forschungszentrum Jülich, Jülich, Germany

Abstract We present a novel Monte-Carlo ice microphysics model, McSnow, to simulate the evolution of ice particles due to deposition, aggregation, riming, and sedimentation. The model is an application and extension of the super-droplet method of Shima et al. (2009) to the more complex problem of rimed ice particles and aggregates. For each individual super-particle, the ice mass, rime mass, rime volume, and the number of monomers are predicted establishing a four-dimensional particle-size distribution. The sensitivity of the model to various assumptions is discussed based on box model and one-dimensional simulations. We show that the Monte-Carlo method provides a feasible approach to tackle this high-dimensional problem. The largest uncertainty seems to be related to the treatment of the riming processes. This calls for additional field and laboratory measurements of partially rimed snowflakes.

1. Introduction

Precipitation in midlatitudes originates mostly from mixed-phase cloud systems and growth of ice particles by the collection of supercooled liquid drops. This process, known as riming, contributes significantly to surface precipitation, see e.g., Grazioli et al. (2015) or Moisseev et al. (2017) for some observational evidence based on state-of-the-art measurement techniques. For example at the coastal areas of Japan, heavily rimed snow particles are in fact present in more than 70% of the snowfall events and contribute more than 50% to wintertime surface precipitation (Harimaya & Sato, 1992a, 1992b). Hence, riming is an important process for the hydrological cycle and can be of similar importance for surface precipitation as growth by condensation or deposition. Riming is also relevant for cloud chemistry due to its impact on phase partitioning (e.g., Kalina & Puxbaum, 1994; Michael & Stuart, 2009; Stuart & Jacobson, 2004).

Measurements and observations of rimed ice crystals have been of interest for decades and observations provide a wealth of data regarding the occurrence of riming and empirical relations of the properties of rimed particles (Fukuta & Takahashi, 1999; Locatelli & Hobbs, 1974; Mitchell et al., 1990; Takahashi & Fukuta, 1988; Takahashi et al., 1991; Zikmunda & Vali, 1972). Most of these measurements use a qualitative classification of particles depending on their degree of riming, e.g., lightly rimed, heavily rimed, graupel-like etc., and provide empirical mass-size or fall speed relations for such rimed particles types. Quantitative measurements of the degree of riming, e.g., in terms of the ratio of rimed mass over total particle mass of individual particles, are rare. The most noteworthy exception is the work of Mosimann et al. (1994). Only recently automatic measurements of the degree of riming are starting to become available (Praz et al., 2017).

Modeling of riming processes is an important part in all mixed-phase cloud models, especially those targeting convective clouds, but only a limited number of modeling studies focus on riming processes. In the early work of Beheng, the stochastic collection equation is explicitly solved for riming processes to study the formation of graupel (Beheng, 1978), the onset of riming (Beheng, 1981) and riming-splintering, i.e., the Hallett-Mossop process (Beheng, 1982, 1987). In Beheng's model of graupel formation and most other spectral bin microphysical models (Flossmann & Wobrock, 2010; Khain et al., 2000, 2015) the size spectra remain one-dimensional, i.e., only the growth in particle mass is calculated and different particle shapes like snow or graupel are described with separate categories and separate size spectra. In such models the conversion from one particle category to another remains somewhat ad hoc and arbitrary. Recently, Jensen and Harrington (2015) and Erfani and Mitchell (2017) have studied riming of individual particles in more detail. To

our knowledge, no spectral bin microphysical model exists that treats the growth by deposition and riming separately in a truly two-dimensional mass distribution, although multidimensional bin models have been used to treat the problem of aerosol particle mass within water droplets and ice particles (Beheng & Herbert, 1986; Bott, 2000; Monier et al., 2006). Morrison and Grabowski (2010) introduced a bin microphysics model of graupel formation with a prognostic rimed mass in each mass bin, which is an improvement over conventional bin schemes, but does not allow different rimed fraction for particles of the same mass, i.e., it does not yet solve the general multidimensional problem.

In bulk microphysical models, riming is often associated with a conversion from snow to graupel and the subsequent growth of graupel into hail. Lacking detailed size information, the conversion rate from snow to graupel in such bulk models is even more arbitrary than in bin microphysics models. Hence, various attempts have been made to introduce additional prognostic variables like a bulk rimed mass or particle volume to overcome these issues (Connolly et al., 2006; Mansell et al., 2010; Milbrandt & Morrison, 2013; Morrison & Grabowski, 2008; Stoelinga et al., 2007). The most advanced bulk approach in this regard is the predicted particle properties (P3) scheme (Milbrandt & Morrison, 2016; Morrison & Milbrandt, 2015; Morrison et al., 2015). Besides mass and number, this scheme predicts the rime mass and the rime volume. Predicting the last two quantities proves to be beneficial or even necessary, because the rime density of particles depends on their growth history and therefore needs to be predicted independently from rime mass. The approach to use multiple prognostic particle properties is very attractive as it can remove many ad hoc parameters related to the snow-to-graupel conversion and reduces the need for a posteriori tuning. This approach is similar in spirit to the habit prediction for primary ice crystals, which mostly aims at the prediction of the different axis growth ratios in different temperature and supersaturation regimes (Chen & Lamb, 1994; Harrington et al., 2013; Hashino & Tripoli, 2007; Jensen et al., 2017). Although the P3 scheme incorporates a more detailed and more physically based description of the riming process compared to other bulk parameterizations, it also comes with several simplifications and assumptions, many of them related to the fact that it is a bulk scheme and cannot resolve the underlying multidimensional particle distribution.

Here, we present a Monte-Carlo microphysical model for the evolution of snow due to depositional growth, aggregation, and riming and the conversion to graupel ("McSnow"), which calculates the evolution of the particle-size distribution in a truly multidimensional microphysical phase space. Similar to the P3 scheme we consider ice mass, rime mass, and rime volume, and in addition we track the number of monomers in the evolution of snow aggregates. In contrast to a bulk model like the P3 scheme, we present a spectrally resolved particle-based description, i.e., we solve for a four-dimensional particle distribution using Monte-Carlo sampling. Numerically this is done using the super-droplet method of Shima et al. (2009) which is applied here for the evolution of multiproperty ice particles. Thus, our model can provide a benchmark simulation to test or falsify certain assumptions made in the bulk approach and develop improved closure assumptions. Additionally, the history of the Lagrangian particles is available, which allows an in-depth analysis of the processes that determine the particle growth within a cloud.

In the current work, we focus on aggregation and riming processes and only ice, snow, and graupel particles are treated by the Monte-Carlo approach. In the one-dimensional model that we use to investigate the basic behavior of the model, we assume for simplicity a fixed bulk description of the cloud water field. A full treatment of the liquid phase and processes like melting, wet growth etc., is beyond the scope of the paper, but is nevertheless a natural extension of McSnow in the future. For now we also do not include a prediction of the aspect ratio or habit of primary ice crystals, but such an extension would be rather straightforward based on the previous work of, for example, Chen and Lamb (1994) and Jensen et al. (2017) and will be included in the future.

Section 2 provides the model description, section 3 presents some box model tests of the numerical convergence, and an analysis of the evolution of the particle-size distribution due to depositional growth, aggregation, and riming in a spatially one-dimensional model. Some conclusions and an outlook are given in section 4.

2. Model Description and Notion of a Super Particle

In McSnow, we assume that an ice particle is an ice crystal which can be completely characterized by an ice crystal mass m_i, a rime mass m_r, a rime volume V_r, and the number of monomers or primary ice crystals n_m,

which a particle might have collected through aggregation. These variables are in the following referred to as the attributes or properties of an ice particle. In the one-dimensional framework, each particle is at any given time completely determined by its four attributes and the current height position z.

The particles-size distribution $f(m_i, m_r, V_r, n_m)$ is the number density of particles in the four dimensional phase space spanned by the particle attributes. Therefore, the particle attributes are sometimes called internal coordinates of the system. For a classic spectral bin model, this space would need to be discretized. Using, for example, 30 bins for each internal coordinate, this would be a discrete system with $30^4 = 810,000$ bins, which immediately shows that this is hardly feasible, especially in combination with a three-dimensional spatial grid. Such high-dimensional systems are more accessible using Monte-Carlo methods. Shima et al. (2009) show that their algorithm is superior to a classic bin approach in phase spaces of degree 3 or higher. All four particle attributes are extensive quantities, i.e., they are additive for successful particle collisions and their total sum is conserved during collision processes.

Our definition of a super particle follows that of Shima et al. (2009) in case of water droplets. A super particle is a representation of multiple ice particles with the same attributes and spatial position. The number of ice particles represented by a super particle is called multiplicity, denoted by η, and may differ from one super particle to another. Since in reality no two different ice particles can have the exact same position and attributes, a super particle is more of a representation of an ensemble of ice particles within a given volume, too small to be further resolved in actual calculations.

2.1. Ice Particle Geometry and Terminal Velocity

In order to implement the Monte-Carlo model, various additional quantities that describe the behavior of ice particles are needed as a function of the chosen particle attributes. In particular, we need to establish relationships between the particle attributes and its diameter and its projected (cross-sectional) area. From that the terminal fall velocity, the collision efficiency and subsequently the gravitational collection kernel can be derived.

For large unrimed particles, we assume that those are aggregates and use the following power law relationships

$$m = \alpha_i D_i^{\beta_i} \tag{1}$$

$$A = \sigma_i D_i^{\gamma_i}, \tag{2}$$

where the coefficients α_i, β_i, σ_i, and γ_i are based on empirical relations for "aggregates of side, planes, columns, and bullets" of Mitchell (1996) and given in Table 1. Such empirical relations are not valid over the whole size range and to avoid unphysical behavior for very small crystals, we assume spherical solid ice particles below a size threshold of

$$D_{\text{th}} = \left(\frac{\pi \rho_i}{6 \alpha_i}\right)^{\frac{1}{\beta_i - 3}}, \tag{3}$$

as it is done in (Morrison & Milbrandt, 2015, equation (8)), where $\rho_i = 997$ kg m^{-3} is the ice density. Aggregation leads to a fractal dimension (exponent of D_i in $m = \alpha_i D_i^{\beta_i}$) of snowflakes close to 2 (Westbrook et al.,

Table 1
Particle-Based m-D and A-D Relations With Constants in MKS Units and the Critical Rime Mass From Equation (5), $m_{\text{th}} = \pi/6 \rho_i D_{\text{th}}^3$, $\alpha_i = 2.8 \times 10^{2\beta_i - 6}$, $\beta_i = 2.1$, $\sigma_i = 2.285 \times 10^{2\gamma_i - 5}$, and $\gamma_i = 1.88$

Ice particle	Type condition	Diameter D	Projected area A
Small ice	$m_r = 0, m_i \leq m_{\text{th}}$	$\left(\frac{6 m_i}{\pi \rho_i}\right)^{1/3}$	$\frac{\pi}{4} D^2$
Unrimed	$m_r = 0, m_i > m_{\text{th}}$	$\left(\frac{m_i}{\alpha_i}\right)^{1/\beta_i}$	$\sigma_i D^{\gamma_i}$
Part. rimed	$m_r < m_{\text{r,crit}}, m_i > m_{\text{th}}$	$\left(\frac{m_i}{\alpha_i}\right)^{1/\beta_i}$	$F_r^* \frac{\pi}{4} D^2 + (1 - F_r^*) \sigma_i D^{\gamma_i}$
Graupel-like	$m_r > m_{\text{r,crit}}$	$\left(\frac{6(m_r - m_{\text{r,crit}})}{\pi \rho_r} + D_i^3\right)^{1/3}$	$\frac{\pi}{4} D^2$

2004a, 2004b) and many empirical relationships for aggregates suggest values very close to 2 or slightly above 2 consistent with this theory (Brown & Francis, 1995; Heymsfield et al., 2010; Mitchell, 1996; Schmitt & Heymsfield, 2010).

To parameterize the transition from a rimed snowflake to graupel, we adopt the "fill-in" model described by Heymsfield (1982). The same approach is used in a bulk formulation in the P3 model of Morrison and Milbrandt (2015, MM15 hereafter). For a partially rimed snowflake, we assume that the maximum dimension does not change until the total volume of the rimed particle is equal to that of a sphere of the same diameter. Hence, the critical rime volume $V_{r,crit}$ can for aggregates be defined as

$$V_{r,crit} = \frac{\pi}{6} D^3 - V_i = \frac{\pi}{6} \left(\frac{m_i}{\alpha_i}\right)^{3/\beta_i} - \frac{m_i}{\rho_i}. \tag{4}$$

If the rime volume is larger than its critical rime volume, we assume that the ice particle takes a spherical form. Similarly, the critical rime mass is defined as

$$m_{r,crit} = \rho_r V_{r,crit} = \rho_r \left\{ \frac{\pi}{6} \left(\frac{m_i}{\alpha_i}\right)^{3/\beta_i} - \frac{m_i}{\rho_i} \right\}, \tag{5}$$

where $\rho_r = m_r / V_r$ is the average rime density of that particle. Above that threshold the particle is spherical and in the following we define those spherical rimed particles as graupel-like independent from their size. Particles with a rimed mass below $m_{r,crit}$ are (partially) rimed snowflakes. The "fill-in" model has two caveats: First, in reality the maximum dimension will start to increase before $m_{r,crit}$ is reached. Second, the "fill-in" model does not provide a consistent estimate for the cross-sectional area. Similar to MM15 we use a linear interpolation of A as a function of the critical rime mass fraction $F_r^* = m_r / m_{r,crit}$ between the unrimed aggregate and the spherical graupel (see Table 1). Note that rimed small ice does immediately convert to graupel, because there is no volume to be filled in. Figure 1 shows the maximum dimension D and the cross-sectional area A as a function of the ice mass and the rime mass for two different rime densities. Most important is that these functions are smooth and have no discontinuities.

With a complete description of the particle geometry at hand, we can now calculate the terminal fall velocity using an aerodynamic model. In the following we apply two slightly different models for the terminal fall velocity. First, we make use of the approach of Khvorostyanov and Curry (2005, KC05 hereafter), which is based on the previous work of Abraham (1970), Beard (1980), Böhm (1989, 1992a), and Mitchell (1996). As an alternative model, we apply the modified Best number approach of Heymsfield and Westbrook (2010, HW10 hereafter). Here, we will shortly repeat the formulation of the two terminal fall velocities.

KC05: The fall velocity is given via the Best number

$$X_B = \frac{2|\rho - \rho_a| V g D^2}{A \eta^2}, \tag{6}$$

and the Reynolds number

$$\mathrm{Re} = \frac{v_t D}{\nu} = \frac{\delta_0^2}{4} \left\{ \left(1 + \frac{4}{\delta_0^2} \sqrt{\frac{X_B}{C_0}} \right)^{1/2} - 1 \right\}^2, \tag{7}$$

using the constants $C_0 = 0.35$ and $\delta_0 = 8$. Here g is the gravitational acceleration, η is the dynamic viscosity, ν is the kinematic viscosity, ρ is the bulk particle density, ρ_a is the density of air, A is the cross-sectional area, and V is the volume of the ice particle given as $V = V_r + m_i / \rho_i$. To account for turbulence effects a modified Reynolds number is used

$$\mathrm{Re}_t = \mathrm{Re}\, \psi^{1/2}(X) = \mathrm{Re} \left\{ \left(1 + \left(\frac{X_B}{X_0} \right)^2 \right) \left(1 + C_t \left(\frac{X_B}{X_0} \right)^2 \right)^{-1} \right\}^{1/2}, \tag{8}$$

and $X_0 = 2.8 \times 10^6$ and $C_t = 1.6$ as suggested in Böhm (1989). The drag coefficient is then calculated from

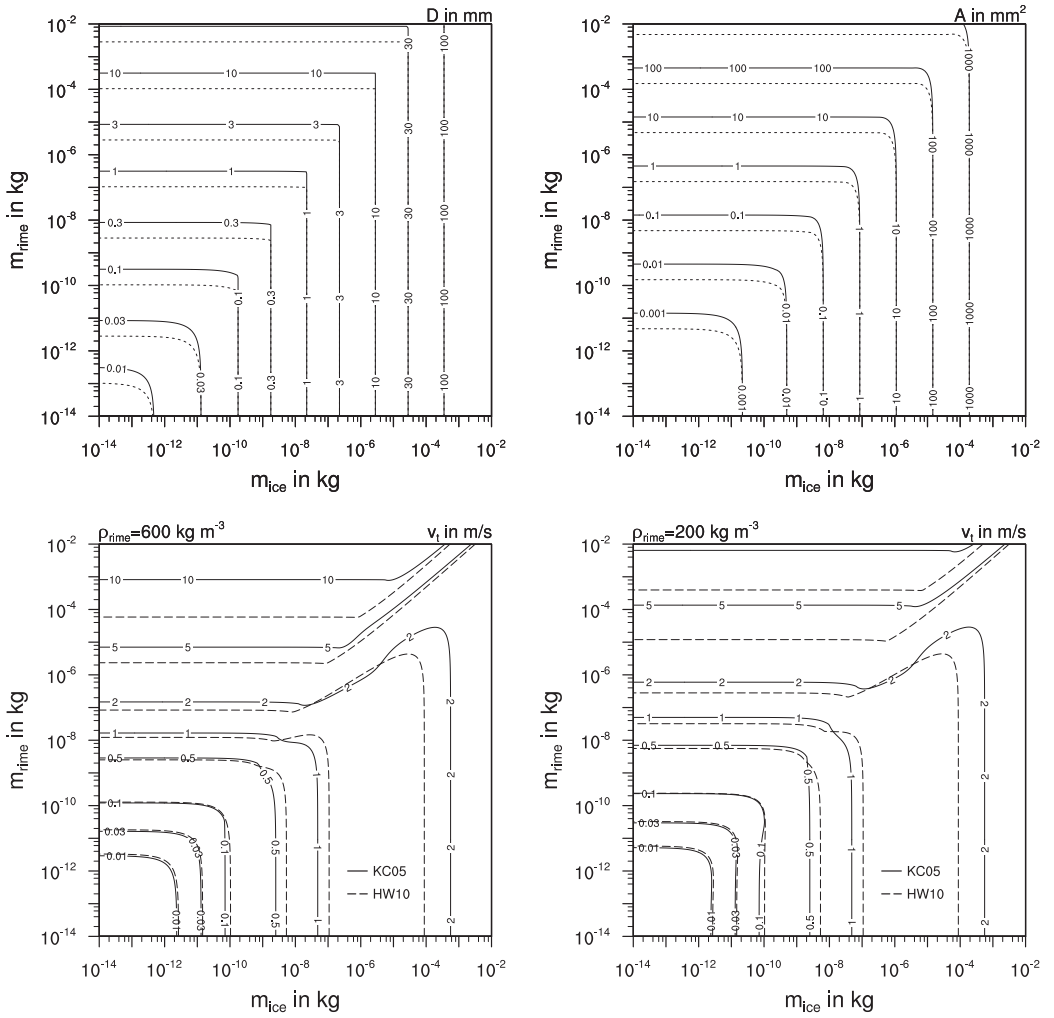

Figure 1. The (top left) *m-D* and (top right) *m-A* relationships with *D* and *A* in mm and mm^2, respectively, for a rime density of 600 kg m^{-3} (solid lines) and 200 kg m^{-3} (dashed lines). The terminal fall velocity in m s^{-1} is shown for two different rime densities of (bottom left) 600 kg m^{-3} and (bottom right) 200 kg m^{-3}, and the two different aerodynamic formulations. The corresponding contours of KC05 and HW10 match well on most parts so that only one of the lines is labeled.

$$C_d = C_0 \left(1 + \frac{\delta_0}{\sqrt{\mathrm{Re}_t}}\right)^2 \psi^{-1}(X). \tag{9}$$

Finally, the fall velocity is given as

$$v_t = \sqrt{\frac{2gV|\rho - \rho_a|}{AC_d\rho_a}}. \tag{10}$$

HW10: Heymsfield and Westbrook introduce the modified Best number

$$X_B^* = \frac{8\rho_a mg}{\pi\eta^2\sqrt{A_r}} \tag{11}$$

with $A_r = \frac{4}{\pi}A/D^2$ and the main difference to the usual definition of X_B is the weaker dependency on *A*. An explicit correction for turbulence effects is not applied in this case and with the Reynolds number as in equation (7) the terminal fall velocity is given directly as

$$v_t = \frac{\eta_a \mathrm{Re}}{\rho_a D} = \frac{\eta_a}{\rho_a D}\frac{\delta_0^2}{4}\left\{\left(1+\frac{4}{\delta_0^2}\sqrt{\frac{X_B^*}{C_0}}\right)^{1/2}-1\right\}^2. \tag{12}$$

In Figure 1, the two m–v_t relationships are plotted in terms of ice crystal mass and rime mass for a high rime density of 600 kg m^{-3} and a low rime density of 200 kg m^{-3}. As expected, the lower rime density results in a lower terminal fall velocity. The KC05 and HW10 velocities differ significantly for particles with large mass, whereas for smaller particles the agreement between both models is quite good.

2.2. Ice Microphysical Processes

Ice particles evolve due to sedimentation, deposition, sublimation, aggregation, and riming. In the following we summarize the equations, parameterizations, and some details of the numerical implementation of these processes in McSnow.

2.2.1. Sedimentation

For a given (super-)particle $S=(x, m_i, m_r, V_r, n_m)$ at time t_0, the sedimentation process transfers it into the (super-)particle $S=(x-v_t(t_1-t_0), m_i, m_r, V_r, n_m)$ at time t_1. In contrast to, for example, Naumann and Seifert (2015), we do not solve the momentum equation for the individual super-particles and assume that all particles attain their terminal velocity instantaneously.

2.2.2. Deposition/Sublimation

In case of an ice crystal particle with mass m, the growth due deposition and sublimation is governed by

$$\frac{\mathrm{d}m}{\mathrm{d}t} = 4\pi C_i D_v f_v \frac{p_v - p_{\mathrm{i,sat}}}{R_v T}\left(1+\frac{L_s^2 D_v p_{\mathrm{i,sat}}}{K_d R_v^2 T^3}\right)^{-1}, \tag{13}$$

where C_i is the capacitance and f_v is the ventilation coefficient of the ice particle, K_d is the thermal conductivity of dry air, D_v is the diffusion coefficient of dry air, L_s is the latent heat of sublimation, R_v is the gas constant of water vapor, T is the air temperature, p_v is the water vapor pressure, and $p_{\mathrm{i,sat}}$ the saturation water pressure over ice. Following Pruppacher and Klett (1997) for graupel-like particles with $m_r > m_{\mathrm{r,crit}}$, we take $C_i = D/2$; for the aggregates with $n_m > 1$, $C_i = D/4$ is taken and in the remaining case, ice particles are assumed to be plate-like with $C_i = D/\pi$. For example, Westbrook et al. (2008) provide further details on the capacitance of ice particles and their results show a weak but significant dependency of C on the number of monomers for aggregates. Here we refrain from introducing such a dependency, because we have no knowledge on the dependency of C on the degree of riming. Combining the methodology of Westbrook et al. (2008) with 3-D particles generated by an aggregation and riming model like the one of Leinonen and Szyrmer (2015), would probably allow to derive such a parameterization in the future. Figure 13 of Westbrook et al. (2008) also shows that discontinuities in C do in fact occur, e.g., between a monocrystal and an aggregate of $n_m = 2$. Therefore, we stick to these rather simple assumptions in this first implementation of McSnow. For the ventilation coefficient, we apply the parameterizations as a function of Reynolds and Schmidt number given by Pruppacher and Klett (1997) for spherical and plate-like ice particles, respectively.

If a particle is rimed and the r.h.s. of (13) is positive, we update only m_i, but not m_r separating rime growth from depositional growth. If the r.h.s. of (13) is negative, the ice crystal part as well as the rime will sublimate. Even though the sublimation acts on the surface of ice particle, we assume that the change in m_i and m_r due to sublimation is proportional to the mass fractions m_i/m and m_r/m, respectively. Hence,

$$\frac{\mathrm{d}m_i}{\mathrm{d}t} = \frac{m_i}{m}\frac{\mathrm{d}m}{\mathrm{d}t}, \qquad \frac{\mathrm{d}m_r}{\mathrm{d}t} = \frac{m_r}{m}\frac{\mathrm{d}m}{\mathrm{d}t}, \qquad \text{for } \frac{\mathrm{d}m_r}{\mathrm{d}t} < 0. \tag{14}$$

If the total mass of a super-particle is nonpositive after the mass update in equation (14), the particle is removed from the system.

2.2.3. Riming

Let us describe the change in m_r and V_r of ice particles when riming with water droplets of a mean radius $\bar{r}_c$ and a liquid water content L_c. Here we describe two alternative approaches, a simple continuous riming model and a stochastic riming, which involves an additional Monte-Carlo sampling of the cloud droplet distribution.

In the continuous riming we solve

$$\frac{\mathrm{d}m_r}{\mathrm{d}t} = \frac{\pi}{4} L_c E_b D^2 v_t, \tag{15}$$

with E_b being the bulk collision efficiency of Cober and List (1993) given as

$$E_b = \max\left(0.55 \ \log_{10}(2.51 K_s), 0\right), \tag{16}$$

with the Stokes number $K_s = 4\rho_{\mathrm{liq}}|\bar{v}_c - v_t|\bar{r}_c^2/(9\eta D)$. Here $\bar{v}_c$ is the fall velocity of the water droplet with radius $\bar{r}_c$ calculated following Beard (1976). The instantaneous rime density ρ_{rime} is given through the impact velocity V_{imp} of Rasmussen and Heymsfield (1985) and the impact parameter $R_{\mathrm{imp}} = -\frac{\bar{r}_c V_{\mathrm{imp}}}{T_s}$. T_s is the temperature on the surface of the ice particle expressed in degree Celsius. Note that Cober and List (1993) define the impact parameter with the impact velocity in m s^{-1} and the droplet radius in μm. Using this empirical parameterization, we arrive at the evolution equation for the rime volume given as

$$\frac{\mathrm{d}V_r}{\mathrm{d}t} = \frac{1}{\rho_{\mathrm{rime}}} \frac{\mathrm{d}m_r}{\mathrm{d}t} \tag{17}$$

with the empirical relation

$$\rho_{\mathrm{rime}} = 78 + 184 R_{\mathrm{imp}} - 15 R_{\mathrm{imp}}^2, \tag{18}$$

which yields ρ_{rime} in kg m^{-3}. Note that the instantaneous rime density ρ_{rime} differs from the bulk rime density ρ_r of a particle, because the latter integrates over the history of the particle and therefore different environmental conditions. The large variation in ρ_{rime} between 100 kg m^{-3} for cold conditions (small R_i) and 600 kg m^{-3} near 0°C (large R_i) is the main reason for needing the additional prognostic variable V_r.

In the stochastic riming, we assume the same probability of finding a water droplet for a given volume of the cloud, which is the case of locally well-mixed clouds. For every ice particle, we compute the number N_d of water droplets in the particle's sweep-out volume according to

$$N_d = \frac{\pi}{4} N_c (D + 2\bar{r}_c)^2 |v_t - \bar{v}_c| \, \Delta t_r, \tag{19}$$

where Δt_r is the model time step used to integrate riming, and $N_c = L_c/(6\bar{m}_d)$ is the number of droplets for a given liquid water content assuming an exponential drop size distribution, $\bar{m}_d$ is the mean cloud droplet mass. Note that we ignore the collision efficiency in this step. Now we introduce a drop multiplicity $\xi_d = N_d/10 + 1$ and draw N_d/ξ_d droplets from the exponential distribution in the size range of 1–40 μm radius. For each droplet we calculate the collision efficiency E_d of Böhm (1992b, 1992c, 1994) for the given pair of particles and update the mass and volume of the ice particle with the increments $m_d E_d \xi_d$ and $m_d E_d \xi_d/\rho_{\mathrm{rime}}$, respectively. Note that the rime density ρ_{rime} is calculated only once per ice particle and time step using the mean cloud droplet diameter.

Which collision efficiency to use is a delicate choice for the riming process. The Cober and List (1993) efficiency has the advantage of being based on actual measurements and it is consistent with their parameterization of the rime density. On the other hand, it is only a bulk efficiency and it is based only on measurements of conical graupel and here we apply it to a much broader range of ice particle habits from unrimed and partially rimed aggregates to spherical graupel. Böhm's parameterization attempts to take the various particle properties like shape, density, and fall speed properly into account, but relies to some extent on semi-empirical assumptions (Böhm, 2004; Posselt et al., 2004). Figure 2 shows both collision efficiencies and clearly reveals that Böhm's collisions efficiency yields significantly higher values compared to Cober and List (1993). This is to be expected, because the Cober and List (1993) provide only a bulk efficiency averaged over the whole cloud droplet distribution and, being based on empirical data, takes into account the surface roughness of rime. von Blohn et al. (2009) show that the Cober and List parameterization tends to underestimate the collision efficiency for spherical graupel by about 25%. Both parameterizations yield significantly lower efficiency for unrimed particles compared to graupel-like particles, which is reasonable.

2.2.4. Aggregation

Two ice particles with attributes $\mathbf{a}_l = (m_{il}, m_{rl}, V_{rl}, n_{ml})$, $l = 1, 2$ aggregate, if successful, into one ice particle with attributes

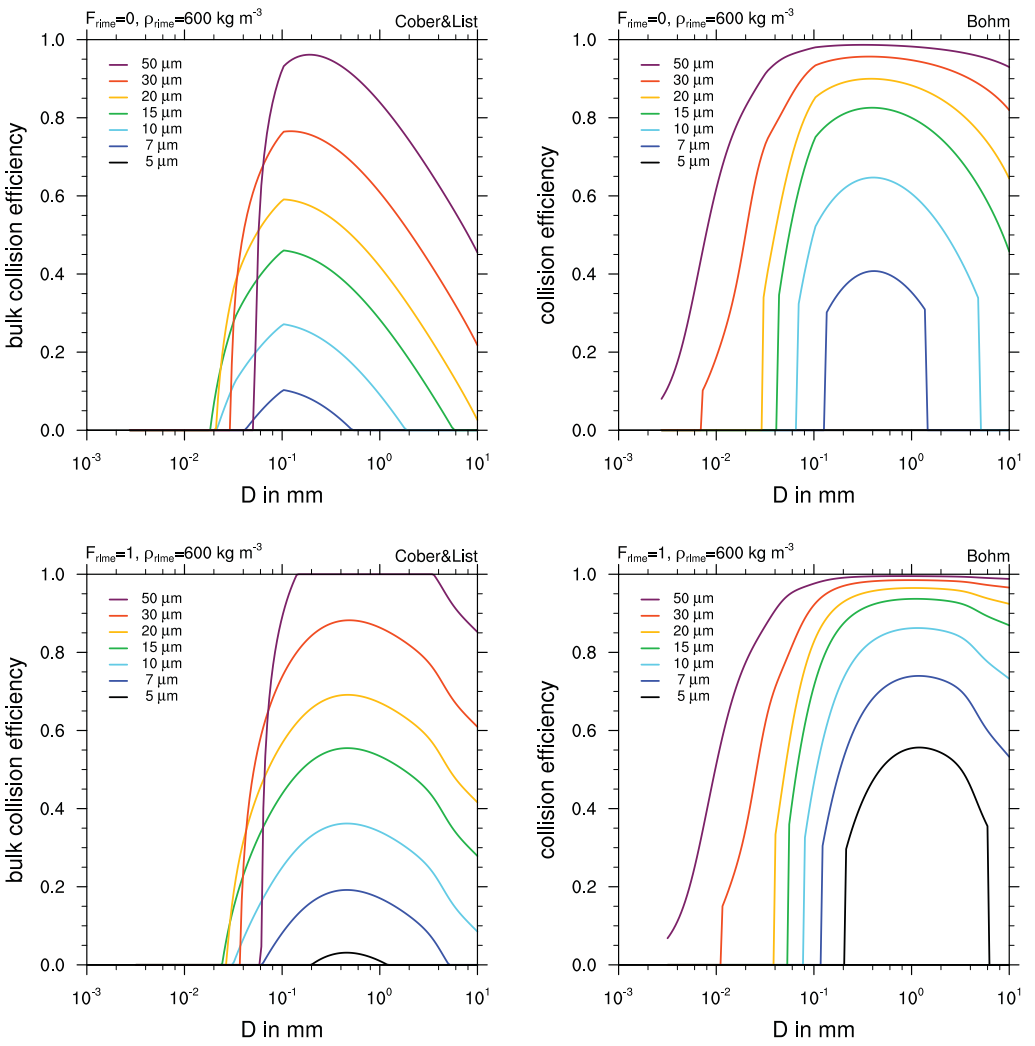

Figure 2. Collision efficiency for the riming of ice particles for (top row) unrimed aggregates ($F_R = 0$) and (bottom row) graupel-like particle ($F_R = 1$ as a function of the maximum dimension of the ice particle for different cloud droplet diameters as indicated by the legend. Shown are the parameterization of (left column) Cober and List and (right column) Böhm. Note that Cober and List provide a bulk collision efficiency for conical graupel, which depend on the mean cloud droplet size, whereas Böhm's efficiency is formulated for individual pairs of particles. Collision efficiencies in this figure are calculated assuming KC05 fall speeds.

$$\mathbf{a}_{12} = \mathbf{a}_1 + \mathbf{a}_2 = (m_{i1} + m_{i2}, m_{r1} + m_{r2}, V_{r1} + V_{r2}, n_{m1} + n_{m2}). \tag{20}$$

A rate of success that two particles aggregate is described by a probability that an ice particle inside a small region ΔV will aggregate in a short time interval $(t, t+\Delta t)$. This probabilistic approach is detailed in Gillespie (1972) and later on in Gillespie (1975) for coalescence of cloud droplets, and can be followed to derive the following probabilistic representation of the classic collection kernel for well-mixed clouds

$$P_{12} = \frac{\pi}{4} (D_1 + D_2)^2 \, |v_1 - v_2| \, E_{\text{coll}} \, \frac{\Delta t}{\Delta V}. \tag{21}$$

Here, E_{coll} is the collision efficiency, which we adopt from a series of papers by Böhm (1989, 1992a, 1992b, 1992c, 1994, 1999) and scale it with a sticking efficiency S_{eff} of ice depending solely on the temperature of the surrounding air (see Pruppacher & Klett, 1997, section 16.2):

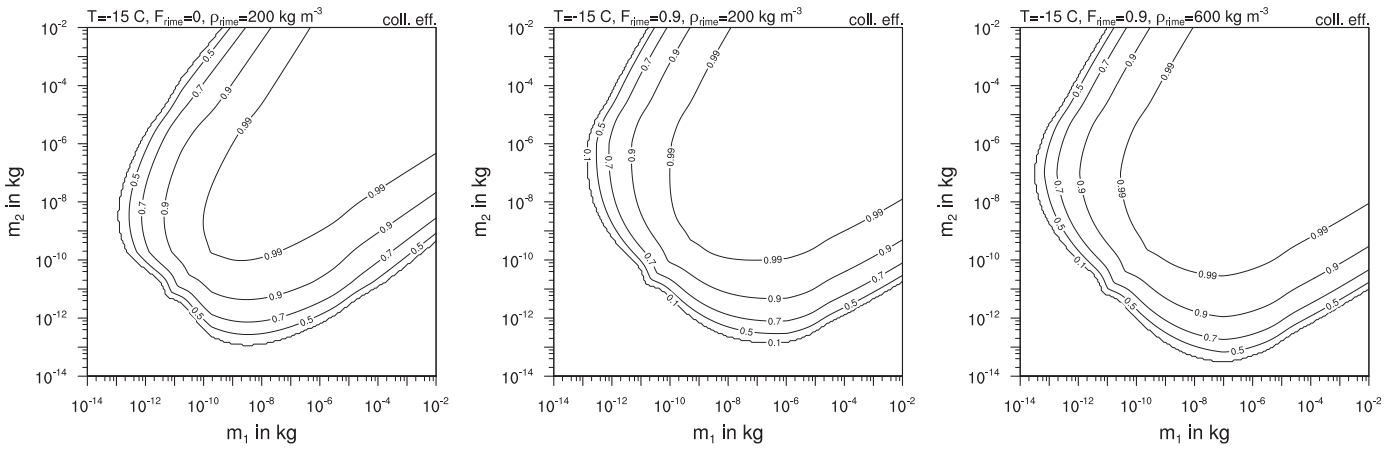

Figure 3. Collision efficiency of Böhm for the collision of unrimed and rimed aggregates as a function of the total mass $m=m_i+m_r$ of each particle. Shown are results for different rime mass fractions $\mathrm{Fr}=m_r/m$ and different bulk rime densities ρ_r with (left) $\mathrm{Fr}=0$, $\rho_r=200$ kg m^{-3}, (middle) $\mathrm{Fr}=0.9$, $\rho_r=200$ kg m^{-3}, and (right) $\mathrm{Fr}=0.9$, $\rho_r=600$ kg m^{-3}.

$$S_{\mathrm{eff}}=\begin{cases}0.10, & T\in[-6,-9]\cup[-4,0]\,^{\circ}\mathrm{C};\\ 0.40, & T\in[-20,-17]\cup[-12.5,-9]\,^{\circ}\mathrm{C};\\ 0.60, & T\in[-9,-6]\,^{\circ}\mathrm{C};\\ 1.00, & T\in[-17,-12.5]\,^{\circ}\mathrm{C};\\ 0.25, & T\in[-60,-20]\,^{\circ}\mathrm{C}.\end{cases}$$

The collision efficiency depends on the geometry and fall speeds of both interacting particles. In our case it is crucial that the parameterization of Böhm provides a continuous model for the dependency of E_{coll} on m_i, m_r, and ρ_r of both particles. In Figure 3, the collision efficiency is shown as a function of the total mass of each particle for different rime mass fractions and for different values of the bulk rime density. For large millimeter-sized ice particles the collision efficiency is close to 1 and only if one of the collision partners is much smaller the collision efficiency becomes small. The dependency of particle properties like rime fraction or rime density is noticeable and should be taken into account.

2.2.5. Aggregation of Super Particles

While the aforementioned sedimentation, depositional growth and riming carry on in a straightforward manner to the super particles, the aggregation is somewhat more involved.

Two super particles S_1 and S_2 aggregate and get replaced with two new super particles S_1' and S_2' such that: (1) in case $\xi_1 > \xi_2$, we have more available particle with the properties S_1 than we have of S_2. Hence, the attributes of S_1 remain unchanged but the multiplicity is reduced to $\xi_1'=\xi_1-\xi_2$. Thus S_1' are the particles of S_1 that do not interact with S_2. Whereas each particle of S_2 aggregates with one from S_1 according to equation (20); and (2) in the special case of $\xi_1=\xi_2$ we want to keep both super particles, if possible. Hence, $[\xi_2/2]$ particles (Throughout this paper the Gauss brackets $[x]$ denote the greatest integer less than or equal to x [the floor function in Fortran]) from S_2 switch to S_1 and aggregate there as in equation (20), whereas the remaining particles of S_1 go to S_2 and aggregate with the remaining particles, making: $\xi_1'=[\xi_2/2]$, $\xi_2'=\xi_2-[\xi_2/2]$. Only if $\xi_1=\xi_2=1$ and therefore $\xi_1'=0$, the super particles S_1' is actually removed from the system.

2.3. Numerical Aspects of the Monte-Carlo Approach

2.3.1. Time Stepping

For efficiency reasons we apply different numerical time steps for the different processes. Let us denote with Δt_s, Δt_d, Δt_r, and Δt_a the time step size for sedimentation, deposition, riming, and aggregation, respectively. We limit the various possibilities of time step sizes to $\Delta t_a=i_{sa}\Delta t_s$, $\Delta t_d=\Delta t_r$, and $\Delta t_s=i_{rs}\Delta t_r$ taking i_{sa}, i_{rs} from the set of natural numbers. At $t+\Delta t_s$ water vapor deposits on an observed super particles, or sublimates from it, according to

$$m_i' = m_i + \Delta t_r \frac{m_i}{m}\,\mathrm{RHS}(t), \qquad m_r' = m_r + \Delta t_r \frac{m_r}{m}\,\min(0, \mathrm{RHS}(t)), \tag{22}$$

where $\mathrm{RHS}(t)$ is the value of the right-hand side expression in equation (13) at time t. The minimum function in the upper equation for m_r indicates that water vapor does not deposit on the rime. Directly after one deposition update, one riming update takes place: new m_r and V_r values are computed either from the continuous riming model, equations (15)–(17), or via the stochastic riming procedure described after equation (19). The deposition and riming updates are repeated i_{rs} times, after which every super particle S moves to its new position $z(t+\Delta t_s) = z(t) - v_t(S)\Delta t_s$. Before the change due to aggregation is applied, the whole previously described combined deposition, riming, and sedimentation process is repeated i_{sa} times. In our numerical experiments, we have seen only negligible differences when applying different $i_{sa} \leq 5$ and $i_{rs} \leq 5$. Therefore, we limit our numerical tests to $i_{sa} = i_{rs} = 1$ in this study.

2.3.2. Monte-Carlo Aggregation

The Lagrangian particle model is largely independent from the Eulerian grid, but for aggregation we have to make a choice which super-particles are close enough to interact. Therefore, the vertical domain is divided into n_z height levels and aggregation is then considered only among those particles which are contained in the same box. Hence, within a height level we make the assumption that particles are well-mixed. Let $I = (S_1, \ldots, S_{N_s})$ be an array of super particles located in a single box. We apply the Monte-Carlo algorithm of Shima et al. (2009) as follows:

1. first a N_s-perturbation $I_p = (Q_1, \ldots, Q_{N_s})$ of the array I is generated with equal probability for every element to occupy every place in the list;
2. for each pair (Q_{2j}, Q_{2j+1}), $j = 1, \ldots, [N_s/2]$, the probability of collision p_j is calculated as

$$p_j = \max(\xi_{2j}, \xi_{2j+1})\, P_j \frac{N_s(N_s-1)}{2} \left[\frac{N_s}{2}\right]^{-1}. \tag{23}$$

With a random number ϕ from uniform distribution on (0,1) this yields the number of collision events

$$\gamma_j = \begin{cases} [p_j]+1, & \text{if } \phi < p_j - [p_j] \\ [p_j], & \text{otherwise.} \end{cases} \tag{24}$$

3. Set $\tilde{\gamma}_j = \min(\gamma_j, [\xi_{2j}/\xi_{2j+1}])$ to prescribe the number of consecutive multiple collisions (mostly due to a large time step size) of the two particles. If $\gamma_j = 0$, the two particles Q_{2i} and Q_{2i+1} do not collide;

if $\gamma_j \neq 0$ and assume $\xi_{2j} > \xi_{2j+1}$, we update the following attributes of Q_j and Q_{j+1}

a) for $\xi_{2j} - \tilde{\gamma}_j \xi_{2j+1} > 0$:

$$\xi_{2j}' = \xi_{2j} - \tilde{\gamma}_j \xi_{2j+1},$$

$$m_{i,2j+1}' = \tilde{\gamma}_j m_{i,2j} + m_{i,2j+1}, \quad m_{r,2j+1}' = \tilde{\gamma}_j m_{r,2j} + m_{r,2j+1},$$

$$V_{r,2j+1}' = \tilde{\gamma}_j V_{r,2j} + V_{r,2j+1},$$

$$n_{m,2j+1}' = \tilde{\gamma}_j n_{m,2j} + n_{m,2j+1}.$$

b) $\xi_{2j} = \tilde{\gamma}_j \xi_{2j+1}$:

$$\xi_{2j}' = [\xi_{2j+1}/2], \qquad \xi_{2j+1}' = \xi_{2j+1} - [\xi_{2j+1}/2],$$

$$m_{i,2j}' = m_{i,2j+1}' = \tilde{\gamma}_j m_{i,2j} + m_{i,2j+1}, \quad m_{r,2j}' = m_{r,2j+1}' = \tilde{\gamma}_j m_{r,2j} + m_{r,2j+1},$$

$$V_{r,2j}' = V_{r,2j+1}' = \tilde{\gamma}_j V_{r,2j} + V_{r,2j+1},$$

$$n_{m,2j}' = n_{m,2j+1}' = \tilde{\gamma}_j n_{m,2j} + n_{m,2j+1}.$$

2.4. Numerical Simulations

As a first step to validate the proposed algorithm, we run box model simulations to assess the convergence of Monte-Carlo for aggregation, similar to Shima et al. (2009). Second, various parameter runs controlling

primarily aggregation and riming are conducted for the 1-D model. The goal of the simulations presented here is mostly to demonstrate the behavior and capabilities of the model. Analytical solutions for validation would only be available for pure aggregation and simplified collision kernels, something which has already been presented by Shima et al. (2009) for liquid drops. For all simulation runs the air motion is excluded. A validation with observations is beyond the scope of the current study.

When evaluating particle-size distributions from a super particle data set $\{S_i : i=\overline{1, N_s}\}$, we resort to the variable density kernel estimate in Terrel and Scott (1992) as suggested by Shima et al. (2009) with

$$f(\ln R)=\frac{1}{V}\sum_{k=1}^{N_s}\xi_k W_\sigma(\ln R-\ln R_k) \tag{25}$$

with the Gaussian kernel W_σ given through

$$W_\sigma(x)=\frac{1}{\sigma\sqrt{2\pi}}\exp\left(-x/2\sigma\right) \tag{26}$$

and $\sigma=\sigma_0 N_s^{0.2}$. $R=D/2$ is the radius of ice particle. Note that the distributions are given in terms of logarithmic radius as in Shima et al. (2009) with their coefficient estimate $\sigma_0=0.62$.

2.4.1. Box Model

In a box model setup, ice (super) particles are confined in a box of volume $V=10^6$ m^3. Two aggregation situations are considered. In the first situation, we consider a fast aggregation with only 210 s before appearance of larger particles. The ice water content is $I_c=1$ g m^{-3} and their number density is set to $N_p=2^{23}$ m$^{-3}=84\times10^5$ m^{-3}. In the second situation we consider a slowly developing aggregation for which $I_c=0.01$ g m^{-3} and $N_p=2\times10^5$ m^{-3} are taken.

We varied the initial multiplicity over $2^k\times10^6$, $k=10,\ldots,1$ which corresponds to the initial number of super particles per volume being 2^k, $k=13,\ldots,22$, respectively. The whole system is integrated until $t=270$ s for the fast and until $t=30,000$ s for the slow aggregation regime. The mass density distributions averaged over 12 runs with different random seeds are shown in Figure 4 every 90 s for the fast aggregation, and in Figure 5 every 10,000 s for the slow aggregation. For both types of developing aggregation, we studied convergence with the HW10 terminal velocity and with the KC05 terminal velocity. Comparing left panels to the right ones in both figures, we can see that HW10 tends to subtly slow down aggregation, although it does produce as large particles as for KC05. Due to the short time frame of fast aggregation, it is generally easier to produce a better converged solution. For fast aggregation the time step size plays a significant role: even for large number of super-particles per volume, we cannot achieve large enough particles as in the case of smaller time steps ($\Delta t=1$ s). For slow aggregation the Monte-Carlo simulation appears to be insensitive to Δt being 1 or 10 s. Quite the opposite is observed for the initial super-particle number per volume N_s. The fast aggregation is relatively insensitive to N_s being 2^{14} m^{-3} or 2^{22} m^{-3}, whereas the slow aggregation is significantly more sensitive to it.

2.4.2. 1-D Model

For the 1-D model we assume an atmosphere as sketched in Figure 6. The gray shaded region above the top-line is where ice particles are initialized on three model levels, in order to create a constant particle flux into the domain. On each level in the boundary zone new ice particles are drawn from an exponential particle-size distribution with a mean mass $\bar{m}=I_{wc}/N_p$, where I_{wc} is the ice water content and N_p is the number density of ice particles. Both I_{wc} and N_p are kept constant in time in this boundary zone. For all 1d test cases, we fix $I_{wc}=10^{-5}$ kg m^{-3} and $N_p=10^5$ m^{-3}. We use $nz=250$ vertical levels, i.e., a vertical grid spacing of 20 m.

Between h_2 and top the ice particles grow by aggregation and by water vapor deposition at a constant supersaturation S_i, which is here set to 2%. Between h_1 and h_2, we assume the presence of a liquid water layer with a (constant) liquid water content of $L_{wc}=0.3$ g m^{-3} in the control simulation. This layer is at water saturation and, hence, has a higher supersaturation over ice than the layer above (right panel of Figure 6). Below the liquid layer the relative humidity is a linear function of height leading to a subsaturation over ice. The temperature decreases linearly with height over the whole profile. Note that liquid water layer as well as the supersaturation is assumed to be constant and is not depleted by riming or the Wegener-Bergeron-Findeisen process. The cloud droplets are treated with a bulk approach and details of treatment of the riming process are given below.

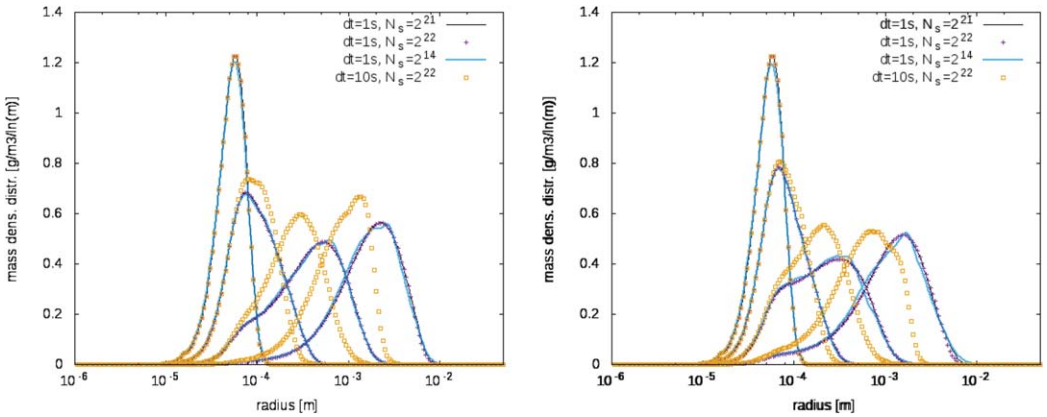

Figure 4. Fast developing aggregation. Convergence of the Monte-Carlo aggregation in the box domain by varying the number of super particles per volume N_s and the time step Δt_a where: (left) the HW10-terminal velocity; (right) the KC05-terminal velocity has been used. Output is every 70 s.

To reach a stationary state we integrate the model over at least 10 h, and all statistical quantities are then averaged over the last 5 h. We apply the continuous riming model and the KC05 terminal fall velocity in this control simulation. Figure 7 shows vertical profiles of some bulk quantities, namely the number and mass density, their fluxes as well as the number of super-particles per grid box and the monomer flux. Profiles are shown for simulations of increasing complexity starting with the trivial case of pure sedimentation (S), which leads to constant profiles in all quantities. Taking into account depositional growth (D) leads to an increase in the mass density and mass flux above h_1. Below h_1 sublimation leads to a loss in mass. The number density decreases (downward) for the SD simulation. This behavior is easily explained by the fact that conservation of particle number corresponds to a constant vertical number density flux, but not necessarily to a constant number density. Due to the increase in particle size the terminal fall velocity increases and the number density decreases corresponding to $F_i = \bar{v}_i N_i =$ const. Hence, the increase in the bulk sedimentation velocity $\bar{v}_i$ leads to a decrease in the number density N_i. For the SD simulation the model conserves particle number until particles sublimate completely at around 200 m above ground. The ice particle number is still conserved when taking into account riming in addition to sedimentation and deposition (labeled "SDR"). Riming leads to a pronounced increase in mass density and mass flux in the liquid layer below h_2, again a moderate decrease in N_i is observed which can be attributed to an increase in particle size and fall speed due to riming. Finally, we take also aggregation into account (labeled "SDRA"). Now the particle number is no longer conserved and we observe a corresponding decrease not only in N_i, but also in the particle flux F_N. The mass density is considerably reduced compared to the SD and SDR simulations due to the size

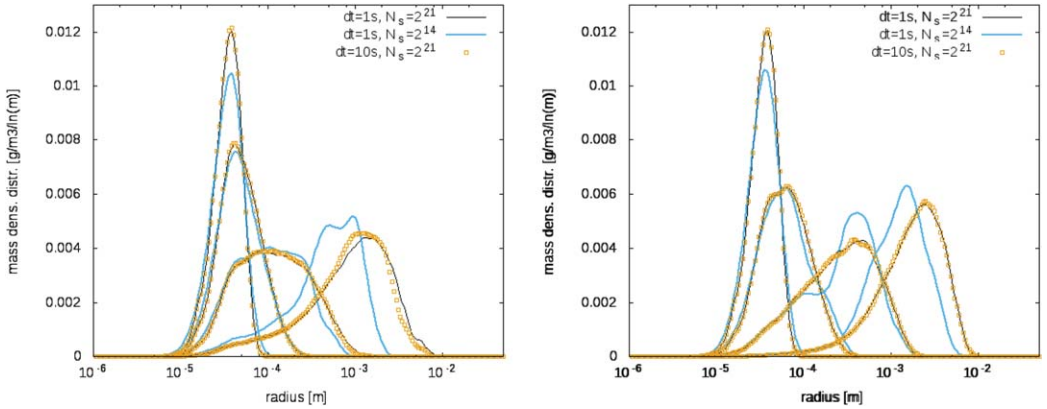

Figure 5. Slowly developing aggregation. Convergence of the Monte-Carlo aggregation in the box domain by varying the number of super particles per volume N_s and the time step Δt_a where: (left) the HW10 terminal velocity; (right) the KC05 terminal velocity has been used. Output is every 8,000 s.

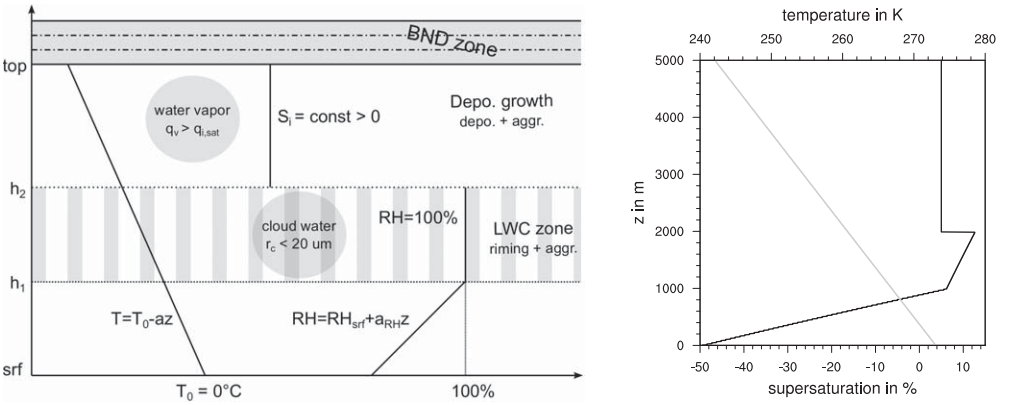

Figure 6. (left) Schematic of background atmosphere for the 1-D model simulations and (right) the vertical profiles of temperature and supersaturation over ice. The temperature and relative humidity profiles, the domain top, and the lower boundary of the riming zone are set fixed with top = 5 km, h_1 = 1 km, h_2 = 2 km, a = 0.0062 K m^{-1} and a_{RH}=0.05% m^{-1}.

growth by aggregation and the corresponding increase in the terminal fall velocity, but also the mass flux is reduced compared to SDR, because particles have less time to grow. Maybe even more important than the increase in fall speed is the fact that many small ice crystals of the SDR simulation have a larger bulk

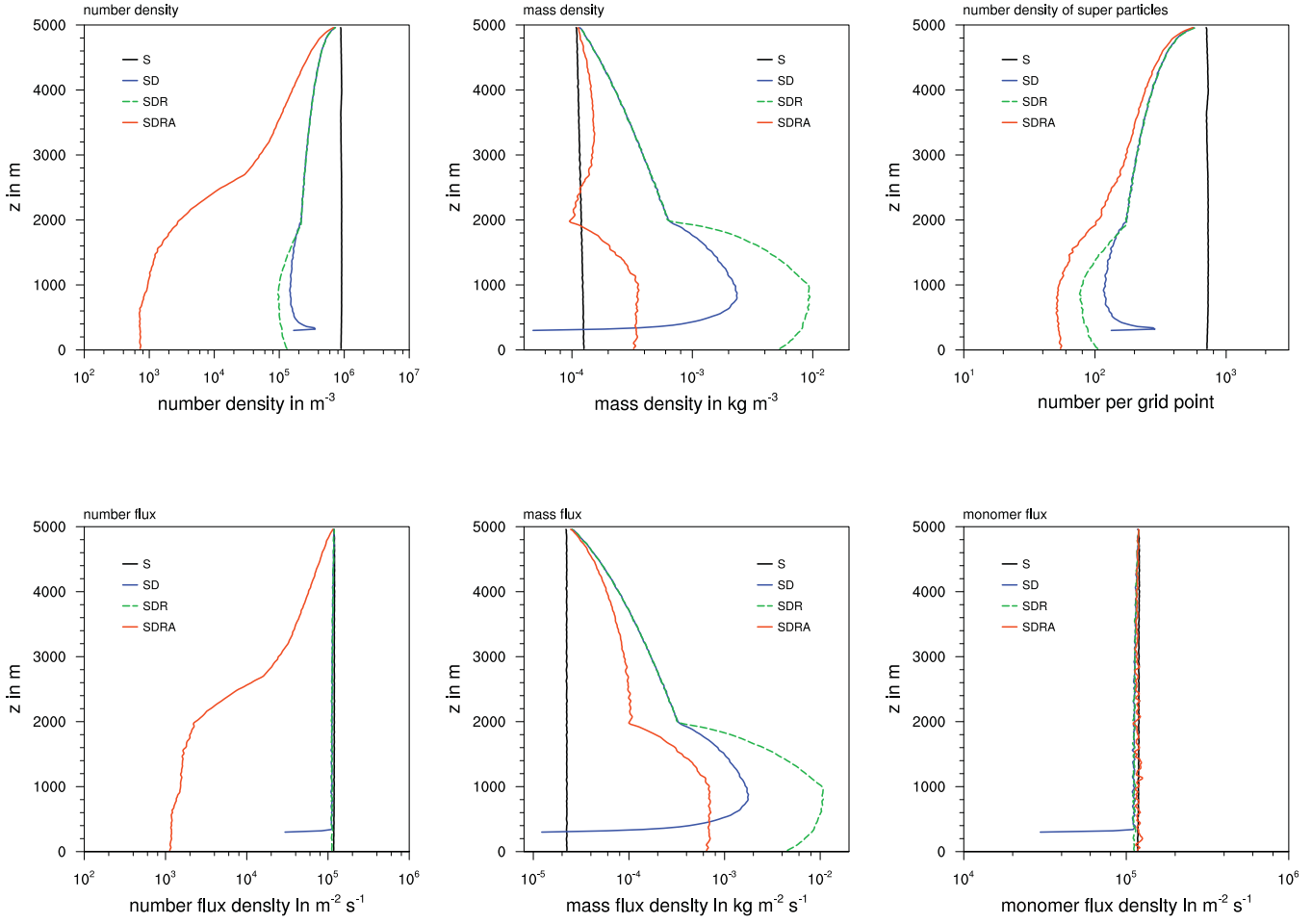

Figure 7. Vertical profiles of the (top left) number density N_i, (top middle) mass density M_i=I_{wc}, (top right) the number of super-particles per grid box N_s, (bottom left) number flux density F_N, (bottom middle) mass flux density F_M, and (bottom right) the monomer flux density F_{mono} for different simulations with individual processes turned on (S: sedimentation, D: water vapor diffusion, A: aggregation, R: riming).

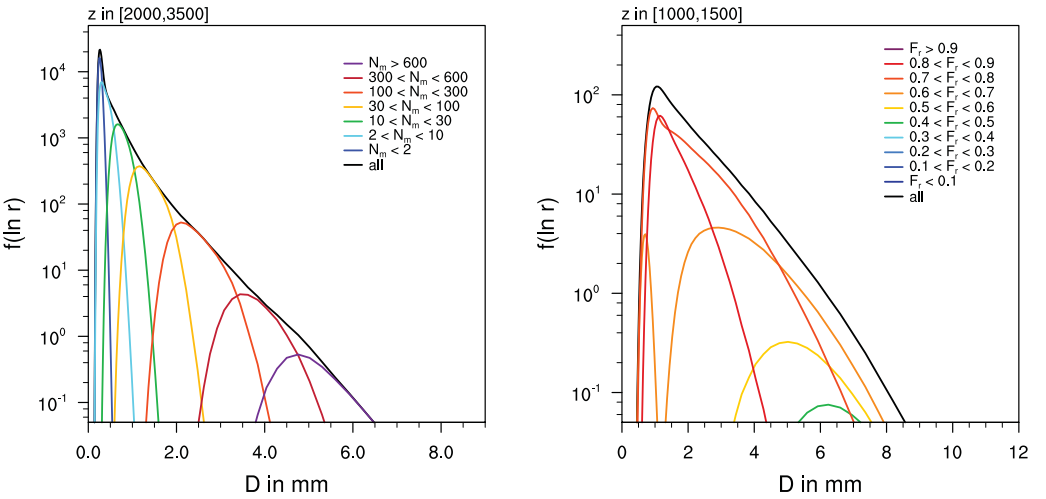

Figure 8. (left) Particle-size distributions in the lower part of the aggregation zone (between 2,000 and 3,500 m height) and (right) in the lower part of the riming zone (between 1,000 and 1,500 m height). In the aggregation zone, the PSD is stratified by the number of monomers of the aggregates n_m, in the riming zone the PSD is stratified by the rime fraction F_r.

deposition rate than fewer, but larger aggregates, which form in the SDRA simulation. Interestingly, the flux density of super-particles per grid box does not decrease when taking into account aggregation. In the Shima algorithm the number of super-particles is conserved as long as all multiplicities remain larger than one. Hence, the profile of N_s is dominated by the increase in terminal fall velocity with particle size and the corresponding decrease in N_s. Even with aggregation the number of monomers is conserved in this system as long as $S_i \geq 0$. The constant monomer flux confirms this conservation property.

The Monte-Carlo particle model provides rich and detailed information about the particle-size distribution. Figure 8 shows the particle-size distribution in the lower part of the aggregation zone and in the lower part of the liquid water layer. In the aggregation zone, we find a distribution with a large number of small ice particles smaller than 0.25 mm diameter and an exponential tail. The distribution is similar to the snow distributions observed, for example, in midlatitude frontal clouds, although not yet strictly bimodal (Field, 2000, 2005). In contrast to a classic bin microphysics model, which would only provide the overall number or mass distribution, the Monte-Carlo models allow a stratification by the number of monomers that compose the aggregates. Hence, we can see that the largest aggregates are built from more than 600 individual crystals, which is a plausible number given that the average monomer size is of order 0.3 mm. The small particle mode corresponds to the remaining primary crystals or monocrystals. Within the riming zone we can stratify the distribution by the degree of riming in terms of $F_r = m_r/(m_i + m_r)$. This shows that the smallest particles are actually most heavily rimed and the large aggregates have a lower degree of riming of $F_r = 0.5$, which corresponds to "densely rimed" using the categorization of Mosimann et al. (1994). Hence, we find small "graupel-like" particles with sizes below 3 mm together with large snowflakes with a lower degree of riming.

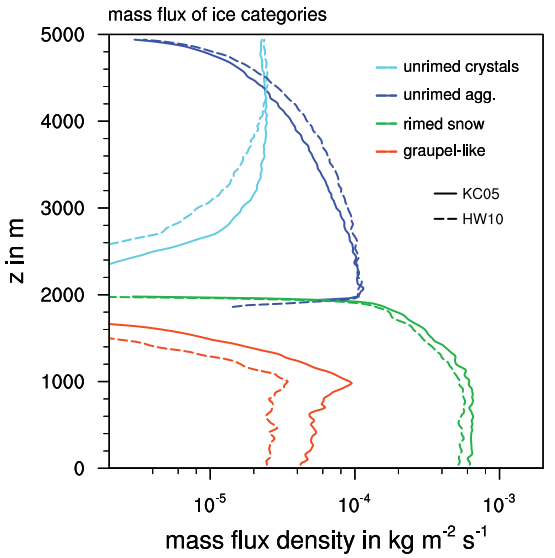

Figure 9. Vertical mass flux profiles comparing two simulations with different formulations of the terminal fall velocity (KC05: solid lines, HW10: dashed). The multidimensional particle-size distribution is categorized into unrimed monocrystals (light blue), unrimed aggregates (dark blue), rimed snow (green), and graupel-like particles (red).

Using the HW10 terminal fall velocity instead of KC05 leads to a more efficient aggregation and a less efficient riming process. This can be seen in Figure 9 in terms of vertical mass fluxes. The mass flux of primary crystals is more quickly depleted by the formation of aggregates when using HW10 compared to KC05 (Figure 10). On the other hand, the mass flux of rimed snow and especially graupel-like particles is

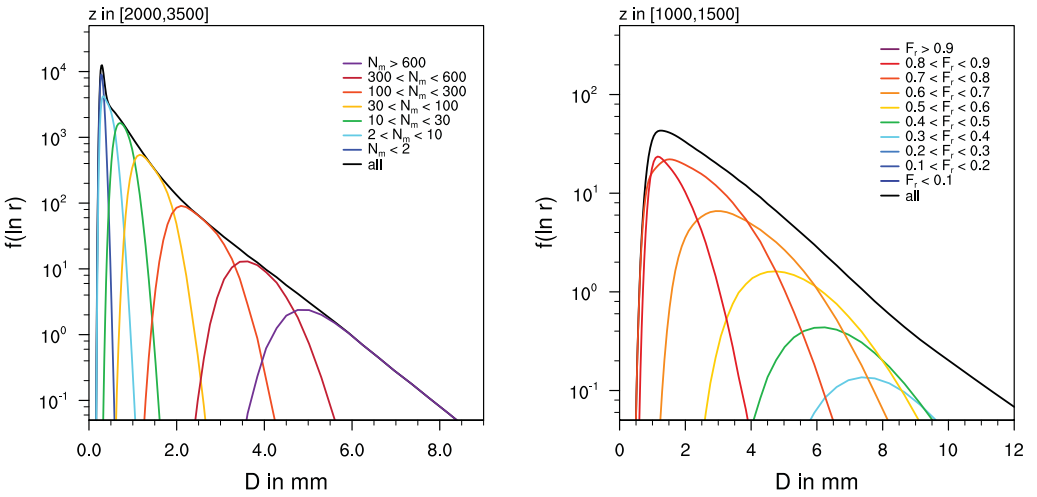

Figure 10. As Figure 8, but for the HW10 fall velocity formulation.

slightly reduced for HW10. This can also be seen in the particle spectra. With HW10 we find more large aggregates in the lower part of the aggregation zone, and those large aggregates show a lower degree of riming. Note that the choice of the terminal fall velocity approach has a more significant impact on aggregation in the 1-D model than in the box model simulations. A possible explanation is an increase in depositional growth due to increased ventilation for large particles in the HW10 case.

Figure 11 shows that vertical profiles of the precipitation rates (mass fluxes) comparing continuous versus stochastic riming. The stochastic riming leads to a more rapid increase of rimed snow in the liquid layer, which is to be expected because the stochastic riming uses the collision efficiencies of Böhm, which are higher than those of Cober and List. The particle-size distribution for stochastic riming, also shown in Figure 11, is very different from the continuous case and here all particle sizes show a rather high degree of riming. Also, this is consistent with Böhm's collision efficiency, which is quite flat for millimeter-sized ice particles. The remarkably different behavior of continuous versus stochastic riming, is thus largely explained by the difference in the collision efficiencies applied in both schemes. Figure 12 shows the sensitivity of both riming models to changes in the mean size of the assumed cloud droplet distribution. Again, we find a remarkably different behavior. For the continuous riming the total mass flux decreases with decreasing mean

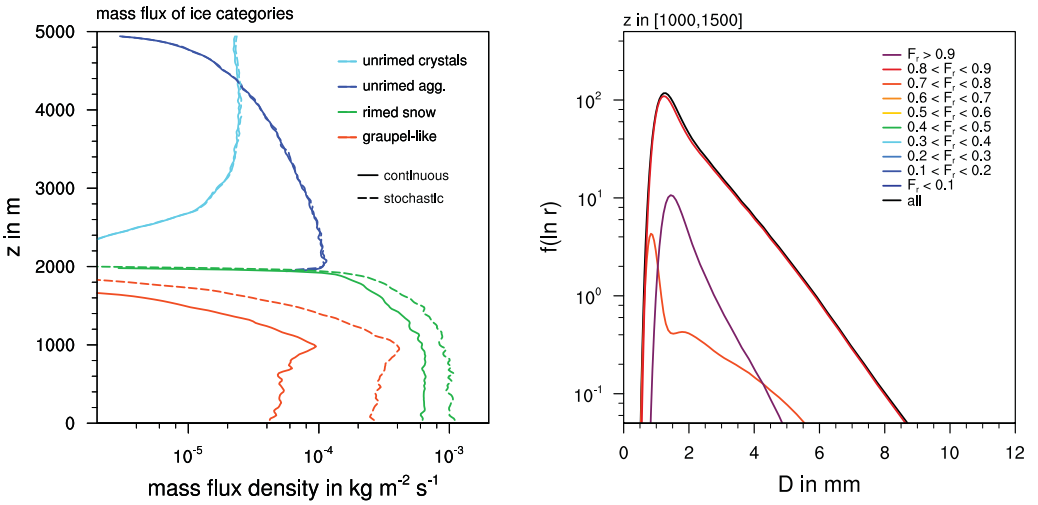

Figure 11. Vertical profiles as in Figure 9, but here for (left) continuous versus stochastic riming, and particle-size distribution in the lower part of the riming zone from the simulation with stochastic riming and (right) using the KC05 fall speed formulation and Böhm's collision efficiency.

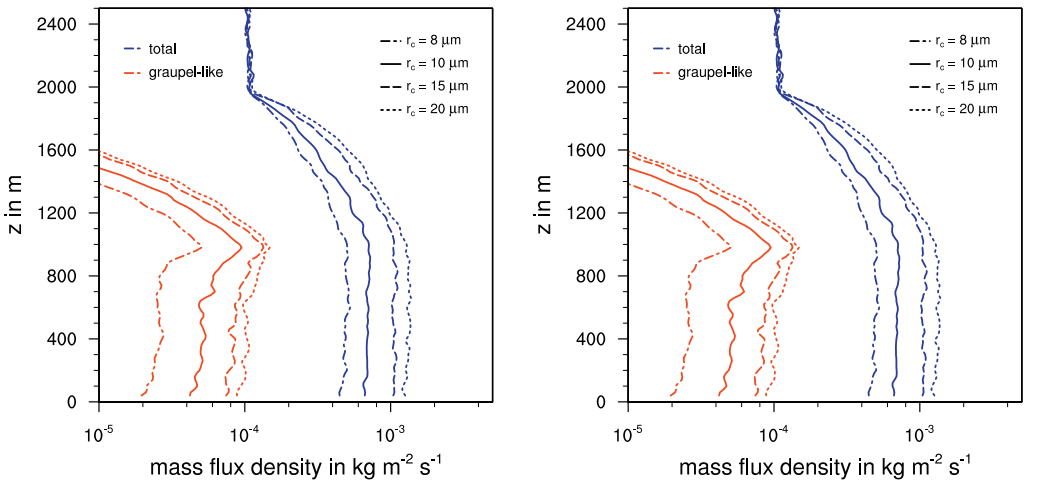

Figure 12. Vertical profiles of the total mass flux and the mass flux of graupel-like particles for different cloud droplet mean radii for the (left) continuous riming model and (right) the stochastic riming model.

droplet size and also the mass flux of graupel-like particle decreases. Both are consistent with the dependency of Cober and List bulk collision efficiency on drop size. For the stochastic riming the total mass flux is insensitive to (moderate) changes in the mean drop size, and the mass flux of graupel-like particles actually increases. The robustness of the total mass flux is again explained by the fact that Böhm's collision efficiency is flat for the larger cloud droplets that dominate the mass gain during riming, i.e., a change in the mean cloud droplet radius has little impact on the rimed mass. For the stochastic riming, the amount of graupel-like particles increases for smaller cloud droplets, which can be explained by that fact that the rime density decreases for smaller droplets and therefore the same amount of rime fills a larger volume making it easier to complete the fill-in stage. For the continuous riming this effect is overruled by the steep decrease in the collision efficiency leading to the opposite behavior.

Based on laboratory measurements of graupel growth von Blohn et al. (2009) argue that the collision efficiencies of Cober and List are about 25% too low for spherical graupel. We have performed additional sensitivity studies with an increased collision efficiency in the continuous growth model and the results remain qualitatively robust (not shown).

Another important but more technical sensitivity is the choice of the number of super-particles used in the simulation. In the 1-D model this is set by the initial multiplicity ξ_0 of the super-particles at the upper boundary condition. Figure 13 shows the vertical profiles of the ice categories derived from the

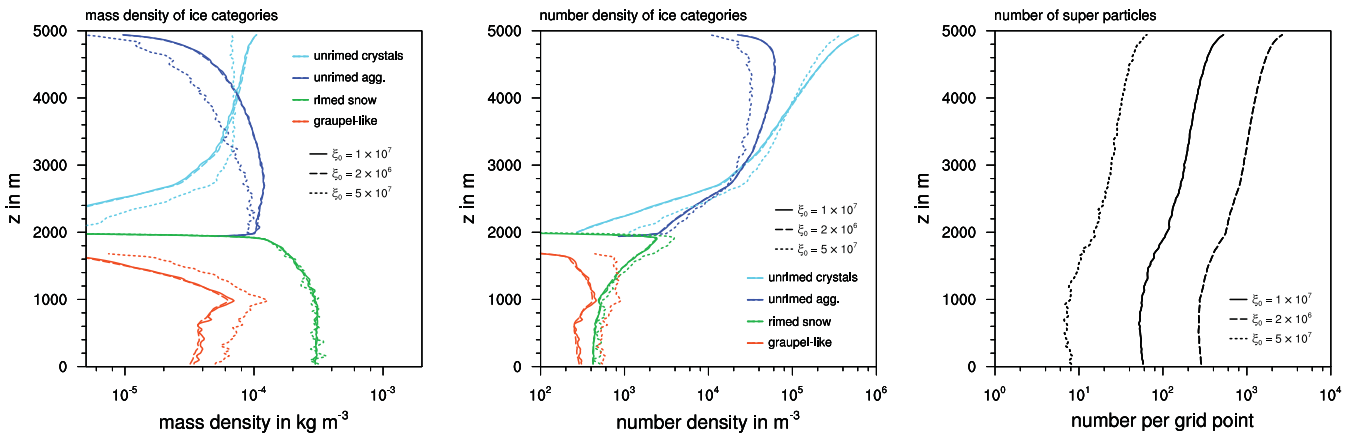

Figure 13. Vertical profiles of the mass density of the (left) ice categories, (middle) their number density, and the total number of super-particles per grid box. Shown are the results of three simulations with different initial multiplicity ξ_0.

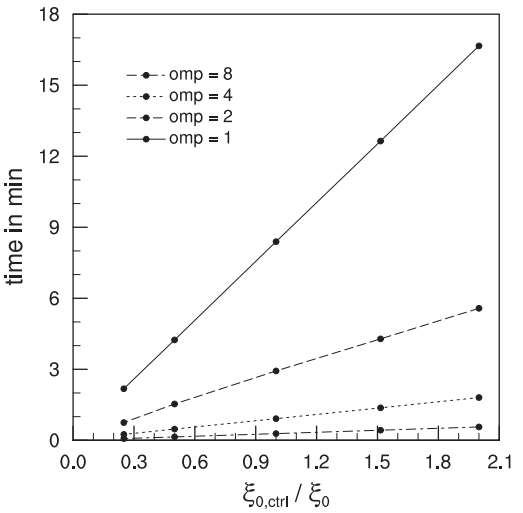

Figure 14. Scaling behavior for the 1-D model. Computing time in minute as a function of (normalized) particle number, $\xi_{0,ctrl}/\xi_0$, for different number of OpenMP threads with $\xi_{0,ctrl}=10^7$.

multidimensional PSD of the control run with $\xi_0=10^7$ and two simulations with initial multiplicities of $\xi_0=2\times10^6$ and $\xi_0=5\times10^7$. The good agreement of the 1-D profiles of the control simulation with $\xi_0=10^7$ and the decreased multiplicity suggests that the control run is already sufficiently converged and this is also confirmed by a comparison of the particle-size distributions (not shown). The simulation with the increased multiplicity deviates significantly from the two other simulations. This under-resolved simulation with $\xi_0=5\times10^7$ suffers from an overestimation of aggregation and an underestimation of riming compared to the benchmark simulation with $\xi_0=2\times10^6$. This suggests that the number of super-particles per grid box should not drop below 10, and one should target 100 super-particles per grid box in the precipitation region, and consequently several hundred in the cloud region, which is dominated by small crystals and slowly sedimenting particles. This is actually not an unreasonably large number given that also a classic bin microphysics model would need more than 100 or even several hundred bins to represent the PSDs of the particle types covered by the multidimensional distribution of McSnow. The higher efficiency of the Monte-Carlo approach for multidimensional phase space is largely due to the fact that the computational cost scales linearly with the number of super-particles (or linearly with $1/\xi_0$). Figure 14 shows this scaling behavior for the 1-D model and proves that the linear scaling with particle number can be found in practice. In addition, we show the speed-up with an OpenMP parallelization of McSnow. This shows that all components of the model, including the collision processes, are reasonably well (and easily) parallelized using OpenMP. This is another advantage of the Monte-Carlo approach.

3. Summary and Conclusions

We have presented a new Monte-Carlo Lagrangian particle model, McSnow, for ice particles with a focus on aggregation and riming processes. The novelty of McSnow is the continuous representation of the transition from (unrimed) snow to graupel on the level of individual Lagrangian particles. This conversion process is usually poorly represented in bulk and bin microphysics models. By Monte-Carlo sampling of the multidimensional particle-size distribution McSnow avoids the use of any predefined particle categories. The multidimensional microphysical phase space in which the particle distribution resides is spanned by the four particle properties mass, rime mass, rime volume, and the number of monomers of the aggregate. Those properties are therefore also called internal coordinates of the particle system.

We have shown that such a model can be derived and implemented using state-of-the-art assumptions and parameterizations, e.g., making use of the fill-in model to describe the geometry of partially rimed snowflakes and using the parameterizations of, for example, Khvorostyanov and Curry for the terminal velocity, Böhm's parameterization of the collision efficiency of aggregates, and empirical relations of Cober and List for the riming efficiency and the rime density. Based on these assumption McSnow simulates reasonable particle-size distributions, which qualitatively resemble observed distributions. The largest uncertainty is probably the choice of the collision efficiency for riming and, closely related to that, the question whether the continuous growth model is sufficiently accurate for riming. A validation or falsification of the different implementations of the riming process might, for example, be possible with in situ measurements of the degree of riming as they were recently presented by Praz et al. (2017) or by using a remote sensing approach to identify riming signatures (Kalesse et al., 2016; Kneifel et al., 2016).

We think that the Monte-Carlo modeling approach used in McSnow opens up new opportunities to study the details of the aggregation and riming processes and their importance for surface precipitation. The model can, to some extent serve as a benchmark to develop and refine certain aspects in bulk parameterization. We hope that McSnow can eventually be helpful to further refine, for example, the P3 approach of Morrison and Milbrandt, which is already formulated in the same spirit in that it avoids the use of

predefined ice categories. Similar efforts to develop and use multidimensional Monte-Carlo models as benchmarking tools have been made in the aerosol community (e.g., Fierce et al., 2017; Riemer et al., 2009). The problem of aerosol particles and their composition has a similar or even higher complexity than cloud microphysics. The Monte-Carlo aerosol particle model of Riemer et al. (2009), for example, uses a 20-dimensional phase space.

The detailed modeling approach of McSnow also shows that our knowledge of the properties of hydrometeors still has significant gaps and additional laboratory work is needed. This is especially true for partially rimed and partially melted particles, although the latter were not discussed in the current study. Eventually, consistent and reliable data of individual particles, and their properties like geometry, terminal fall velocity, capacitance, sticking efficiency, ventilation coefficients, etc., as a function of the aforementioned internal coordinates is needed. More generally this should, of course, be extended to include various habits of primary crystals, e.g., following the work of Chen and Lamb (1994) and Jensen et al. (2017).

Eventually a validation of McSnow with detailed observations is necessary, for example, to decide which implementation of the riming process is more realistic. To do this we will implement McSnow into the three-dimensional ICON model (Zängl et al., 2015) to be able to perform case studies of actual snow events. We will report on this endeavor in future publications.

Acknowledgments
The authors thank the German Federal Ministry of Education and Research (BMBF) for funding this project as part of the HD(CP)^2 research program under grant 01LK1505B. Both authors thank Shin-ichiro Shima for sharing his super-droplet code in the early stage of our development. We thank Vaughan Phillips and Martin Simmel for making their implementations of Böhm's collision efficiency available to us. We thank Christoph Siewert, who carefully reviewed the code of McSnow and identified several bugs. We acknowledge the computing time on JURECA at the research center Jülich. McSnow source code is available from https://gitlab.com/sbrdar/mcsnow after access has been granted by the authors.

References

Abraham, F. (1970). Functional dependence of drag coefficient of a sphere on Reynolds number. *Physics of Fluids*, *13*, 2194–2195.
Beard, K. V. (1976). Terminal velocity and shape of cloud and precipitation drops aloft. *Journal of Atmosphere Sciences*, *33*, 851–864.
Beard, K. V. (1980). The effects of altitude and electrical force on the terminal velocity of hydrometeors. *Journal of Atmosphere Sciences*, *37*, 1363–1374.
Beheng, K. D. (1978). Numerical simulation of graupel development. *Journal of Atmosphere Sciences*, *35*, 683–689.
Beheng, K. D. (1981). Stochastic riming of plate-like and columnar ice crystals. *Pure and Applied Geophysics*, *119*, 820–830.
Beheng, K. D. (1982). A numerical study on the combined action of droplet coagulation, ice particle riming and the splintering process concerning maritime cumuli. *Contributions to Atmospheric Physics*, *55*, 201–214.
Beheng, K. D. (1987). Microphysical properties of glaciating cumulus clouds: Comparison of measurements with a numerical simulation. *Quarterly Journal of the Royal Meteorological Society*, *119*, 1377–1382.
Beheng, K. D., & Herbert, F. (1986). Mathematical studies on the aerosol concentration in drops changing due to particle scavenging and redistribution by coagulation. *Meteorology and Atmospheric Physics*, *35*, 212–219.
Böhm, J. P. (1989). A general equation for the terminal fall speed of solid hydrometeors. *Journal of Atmosphere Sciences*, *46*, 253–274.
Böhm, J. P. (1992a). A general hydrodynamic theory for mixed-phase microphysics. Part I. Drag and fall speed of hydrometeors. *Atmospheric Research*, *27*, 253–274.
Böhm, J. P. (1992b). A general hydrodynamic theory for mixed-phase microphysics. Part II. Colision kernels for coalescence. *Atmospheric Research*, *27*, 275–290.
Böhm, J. P. (1992c). A general hydrodynamic theory for mixed-phase microphysics. Part III. Riming and aggregation. *Atmospheric Research*, *28*, 103–123.
Böhm, J. P. (1994). Theoretical collision efficiencies for riming and aerosol impaction. *Atmospheric Research*, *32*, 171–187.
Böhm, J. P. (1999). Revision and clarification of "A general hydrodynamic theory for mixed-phase microphysics". *Atmospheric Research*, *52*, 167–176.
Böhm, J. P. (2004). Reply to comment on "Revision and clarification of 'A general hydrodynamic theory for mixed-phase microphysics' [Böhm J.P., 1999, Atmos. Res. 52, 167–176]". *Atmospheric Research*, *69*, 289–293.
Bott, A. (2000). A flux method for the numerical solution of the stochastic collection equation: extension to two-dimensional particle distributions. *Journal of Atmosphere Sciences*, *57*, 284–294.
Brown, P. R. A., & Francis, P. N. (1995). Improved measurements of the ice water content in cirrus using a total-water probe. *Journal of Atmospheric and Oceanic Technology*, *12*, 410–414.
Chen, J.-P., & Lamb, D. (1994). Simulation of cloud microphysical and chemical processes using a multicomponent framework. *Journal of Atmosphere Sciences*, *51*, 2613–2630.
Cober, S. G., & List, R. (1993). Measurements of the heat and mass transfer parameters characterizing conical graupel growth. *Journal of Atmosphere Sciences*, *50*, 1591–1609.
Connolly, P. J., Choularton, T. W., Gallagher, M. W., Bower, K. N., Flynn, M. J., & Whiteway, J. A. (2006). Cloud-resolving simulations of intense tropical Hector thunderstorms: Implications for aerosol-cloud interactions. *Quarterly Journal of the Royal Meteorological Society*, *132*, 3079–3106.
Erfani, E., & Mitchell, D. L. (2017). Growth of ice particle mass and projected area during riming. *Atmospheric Chemistry and Physics*, *17*, 1241–1257.
Field, P. R. (2000). Bimodal ice spectra in frontal clouds. *Quarterly Journal of the Royal Meteorological Society*, *126*, 379–392.
Field, P. R. (2005). Parametrization of ice-particle-size distributions for mid-latitude stratiform cloud. *Quarterly Journal of the Royal Meteorological Society*, *131*, 1997–2017.
Fierce, L., Riemer, N., & Bond, T. C. (2017). Toward reduced representation of mixing state for simulating aerosol effects on climate. *Bulletin of the American Meteorological Society*, *98*, 971–980.
Flossmann, A. I., & Wobrock, W. (2010). A review of our understanding of the aerosol-cloud interaction from the perspective of a bin resolved cloud scale modelling. *Atmospheric Research*, *97*, 478–497.
Fukuta, N., & Takahashi, T. (1999). The growth of atmospheric ice crystals: A summary of findings in vertical supercooled cloud tunnel studies. *Journal of Atmosphere Sciences*, *56*, 1963–1979.

Gillespie, D. T. (1972). The stochastic coalescence model for cloud droplet growth. *Journal of Atmosphere Sciences*, *29*, 1496–1510.
Gillespie, D. T. (1975). An exact method for numerically simulating the stochastic coalescence process in a cloud. *Journal of Atmosphere Sciences*, *32*, 1977–1989.
Grazioli, J., Lloyd, G., Panziera, L., Hoyle, C. R., Connolly, P. J., Henneberger, J., & Berne, A. (2015). Polarimetric radar and in situ observations of riming and snowfall microphysics during CLACE 2014. *Atmospheric Chemistry and Physics*, *15*, 13787–13802.
Harimaya, T., & Sato, M. (1992a). Measurement of the riming amount on snowflakes. *Journal of the Faculty of Science, Hokkaido University*, *8*, 355–366.
Harimaya, T., & Sato, M. (1992b). The riming proportion of snow particles falling in coastal areas. *Journal of the Meteorological Society of Japan*, *70*, 57–65.
Harrington, J. Y., Sulia, S., & Morrison, H. (2013). A method for adaptive habit prediction in bulk microphysical models. Part I: Theoretical development. *Journal of Atmosphere Sciences*, *70*, 349–364.
Hashino, T., & Tripoli, G. J. (2007). The spectral ice habit prediction system (SHIPS). Part I: Model description and simulation of the vapor deposition process. *Journal of Atmosphere Sciences*, *64*, 2210–2237.
Heymsfield, A. J. (1982). A comparative study of the rates of development of potential graupel and hail embryos in high plains storms. *Journal of Atmosphere Sciences*, *39*, 2867–2897.
Heymsfield, A. J., Schmitt, C., Bansemer, A., & Twohy, C. H. (2010). Improved representation of ice particle masses based on observations in natural clouds. *Journal of Atmosphere Sciences*, *67*, 3303–3318.
Heymsfield, A. J., & Westbrook, C. D. (2010). Advances in the estimation of ice particle fall speed using laboratory and field measurements. *Journal of Atmosphere Sciences*, *67*, 2469–2482.
Jensen, A. A., & Harrington, J. Y. (2015). Modeling ice crystal aspect ratio evolution during riming: A single-particle growth model. *Journal of Atmosphere Sciences*, *72*, 2569–2590.
Jensen, A. A., Harrington, J. Y., Morrison, H., & Milbrandt, J. A. (2017). Predicting ice shape evolution in a bulk microphysics model. *Journal of Atmosphere Sciences*, *74*, 2081–2104.
Kalesse, H., Szyrmer, W., Kneifel, S., Kollias, P., & Luke, E. (2016). Fingerprints of a riming event on cloud radar Doppler spectra: Observations and modeling. *Atmospheric Chemistry and Physics*, *16*, 2997–3012.
Kalina, M. F., & Puxbaum, H. (1994). A study of the influence of riming of ice crystals on snow chemistry during different seasons in precipitating continental clouds. *Atmospheric Environment*, *28*, 3311–3328.
Khain, A., Beheng, K. D., Heymsfield, A., Korolev, A., Krichak, S. O., Levin, Z., . . . Yano, J.-I. (2015). Representation of microphysical processes in cloud-resolving models: Spectral (bin) microphysics versus bulk parameterization. *Reviews of Geophysics*, *53*, 247–322. https://doi.org/10.1002/2014RG000468
Khain, A., Ovtchinnikov, M., Pinsky, M., Pokrovsky, A., & Krugliak, H. (2000). Notes on the state-of-the-art numerical modeling of cloud microphysics. *Atmospheric Research*, *55*, 159–224.
Khvorostyanov, V. I., & Curry, J. A. (2005). Fall velocities of hydrometeors in the atmosphere: Refinements to a continuous analytical power law. *Journal of Atmosphere Sciences*, *62*, 4343–4357.
Kneifel, S., Kollias, P., Battaglia, A., Leinonen, J., Maahn, M., Kalesse, H., & Tridon, F. (2016). First observations of triple-frequency radar Doppler spectra in snowfall: Interpretation and applications. *Geophysical Research Letters*, *43*, 2225–2233. https://doi.org/10.1002/2015GL067618
Leinonen, J., & Szyrmer, W. (2015). Radar signatures of snowflake riming: A modeling study. *Earth and Space Science*, *2*, 2333–5084.
Locatelli, J. D., & Hobbs, P. V. (1974). Fall speeds and masses of solid precipitation particles. *Journal of Geophysical Research*, *79*, 2185–2197. https://doi.org/10.1029/JC079i015p02185
Mansell, E. R., Ziegler, C. L., & Bruning, E. C. (2010). Simulated electrification of a small thunderstorm with two-moment bulk microphysics. *Journal of Atmosphere Sciences*, *67*, 171–194.
Michael, R., & Stuart, A. L. (2009). The fate of volatile chemicals during wet growth of a hailstone. *Environmental Research Letters*, *4*, 015001.
Milbrandt, J. A., & Morrison, H. (2013). Prediction of graupel density in a bulk microphysics scheme. *Journal of the Atmospheric Sciences*, *70*, 410–429.
Mitchell, D. L. (1996). Use of mass- and area-dimensional power laws for determining precipitation particle terminal velocities. *Journal of Atmosphere Sciences*, *53*, 1710–1723.
Mitchell, D. L., Zhang, R., & Pitter, R. L. (1990). Mass-dimensional relationships for ice particles and the influence of riming on snowfall rates. *Journal of Applied Meteorology*, *29*, 153–163.
Moisseev, D., von Lerber, A., & Tiira, J. (2017). Quantifying the effect of riming on snowfall using ground-based observations. *Journal of Geophysical Research: Atmospheres*, *122*, 4019–4037. https://doi.org/10.1002/2016JD026272
Monier, M., Wobrock, W., Gayet, J.-F., & Flossmann, A. (2006). Development of a detailed microphysics cirrus model tracking aerosol particles' histories for interpretation of the recent INCA campaign. *Journal of Atmosphere Sciences*, *63*, 504–525.
Morrison, H., & Grabowski, W. W. (2008). A novel approach for representing ice microphysics in models: Description and tests using a kinematic framework. *Journal of Atmosphere Sciences*, *65*, 1528–1548.
Morrison, H., & Grabowski, W. W. (2010). An improved representation of rimed snow and conversion to graupel in a multicomponent bin microphysics scheme. *Journal of Atmosphere Sciences*, *67*, 1337–1360.
Morrison, H., & Milbrandt, J. A. (2015). Parameterization of cloud microphysics based on the prediction of bulk ice particle properties. Part I: Scheme description and idealized tests. *Journal of Atmosphere Sciences*, *72*, 287–311.
Morrison, H., Milbrandt, J. A., Bryan, G. B., Ikeda, K., Tessendorf, S. A., & Thompson, G. (2015). Parameterization of cloud microphysics based on the prediction of bulk ice particle properties. Part II: Case study comparisons with observations and other schemes. *Journal of Atmosphere Sciences*, *72*, 312–339.
Mosimann, L., Weingartner, E., & Waldvogel, A. (1994). An analysis of accreted drop sizes and mass on rimed snow crystals. *Journal of Atmosphere Sciences*, *51*, 1548–1558.
Naumann, A. K., & Seifert, A. (2015). A Lagrangian drop model to study warm rain microphysical processes in shallow cumulus. *Journal of Advances in Modeling Earth Systems*, *7*, 1136–1154. https://doi.org/10.1002/2015MS000456
Posselt, R., Simmel, M., & Wurzler, S. (2004). Comment on "Revision and clarification of 'A general hydrodynamic theory for mixed-phase microphysics' [Böhm, J.P., 1999, Atmos. Res. 52, 167–176]". *Atmospheric Research*, *69*, 281–287.
Praz, C., Roulet, Y.-A., & Berne, A. (2017). Solid hydrometeor classification and riming degree estimation from pictures collected with a Multi-Angle Snowflake Camera. *Atmospheric Measurement Techniques*, *10*, 1335–1357.
Pruppacher, H. R., & Klett, J. D. (1997). *Microphysics of clouds and precipitation, second revised and enlarged edition with an introduction to cloud chemistry and cloud electricity*. Dordrecht, the Netherlands: Kluwer Academic.

Rasmussen, R. M., & Heymsfield, A. J. (1985). A generalized form for impact velocities used to determine graupel accretional densities. *Journal of Atmosphere Sciences*, *42*, 2275–2279.

Riemer, N., West, M., Zaveri, R. A., & Easter, R. C. (2009). Simulating the evolution of soot mixing state with a particle-resolved aerosol model. *Journal of Geophysical Research*, *114*, D09202. https://doi.org/10.1029/2008JD011073

Schmitt, C. G., & Heymsfield, A. J. (2010). The dimensional characteristics of ice crystal aggregates from fractal geometry. *Journal of Atmosphere Sciences*, *67*, 1605–1616.

Shima, S., Kusano, K., Kawano, T., Sugiyama, T., & Kawahara, S. (2009). The super-droplet method for the numerical simulation of clouds and precipitation: A particle-based and probabilistic microphysics model coupled with a non-hydrostatic model. *Quarterly Journal of the Royal Meteorological Society*, *135*, 1307–1320.

Stoelinga, M., McCormick, H., & Locatelli, J. D. (2007). *Prediction of degree of riming within a bulk microphysical scheme*. Paper presented at 22nd Conference on Weather Analysis and Forecasting/18th Conference on Numerical Weather Prediction. U.S. Naval Research Laboratory, Monterey, CA.

Stuart, A. L., & Jacobson, M. Z. (2004). Chemical retention during dry growth riming. *Quarterly Journal of the Royal Meteorological Society*, *135*, 1307–1320.

Takahashi, T., Endoh, T., Wakahama, G., & Fukuta, N. (1991). Vapor diffusional growth of free-falling snow crystals between −3 and −23°C. *Journal of the Meteorological Society of Japan*, *69*, 15–30.

Takahashi, T., & Fukuta, N. (1988). Super cooled cloud tunnel studies on the growth of snow crystals between −4 and −20°C. *Journal of the Meteorological Society of Japan*, *66*, 841–855.

Terrel, G. R., & Scott, D. W. (1992). Variable kernel density estimation. *Annals of Statistics*, *20*, 1236–1265.

von Blohn, N., Diehl, K., Mitra, S. K., & Borrmann, S. (2009). Riming of graupel: Wind tunnel investigations of collection kernels and growth regimes. *Journal of the Atmospheric Sciences*, *66*, 2359–2366.

Westbrook, C. D., Ball, R. C., Field, P. R., & Heymsfield, A. J. (2004a). Theory of growth by differential sedimentation, with application to snowflake formation. *Physical Review E*, *70*, 021403.

Westbrook, C. D., Ball, R. C., Field, P. R., & Heymsfield, A. J. (2004b). Universality in snowflake aggregation. *Geophysical Research Letters*, *31*, L15104. https://doi.org/10.1029/2004GL020363

Westbrook, C. D., Hogan, R. J., & Illingworth, A. J. (2008). The capacitance of pristine ice crystals and aggregate snowflakes. *Journal of Atmosphere Sciences*, *65*, 206–219.

Zängl, G., Reinert, D., Rípodas, P., & Baldauf, M. (2015). The ICON (ICOsahedral Non-hydrostatic) modelling framework of DWD and MPI-M: Description of the non-hydrostatic dynamical core. *Quarterly Journal of the Royal Meteorological Society*, *141*, 563–579.

Zikmunda, J., & Vali, G. (1972). Fall patterns and fall velocities of rimed ice crystals. *Journal of Atmosphere Sciences*, *29*, 1334–1347.